AIAA Aviation
22-26 June 2015, Dallas, TX
21st AIAA/CEAS Aeroacoustics Conference

21st AIAA/CEAS Aeroacoustic Conference, June 2015, Dallas, Texas

Installation noise of a turbofan jet engine under an airfoil

Gwendoline Brichet*, Maxime Kœnig†
Safran Snecma, Acoustics Department, Moissy-Cramayel, France
Christophe Bailly‡
Ecole Centrale de Lyon, 36 Avenue Guy de Collongue, 69134 Ecully Cedex, France

Excess noise induced by installation effects are numerically investigated in this work. A realistic turbofan jet engine placed under a NACA0012 profile is considered. Experimental data, regarding the turbulent flow and its acoustics, are indeed available. A RANS simulation is used as input data in an acoustic statistical model to predict mixing noise generated by an isolated jet. This model however needs to be revisited to include installation effects. In order to take account of the presence of the wing, the linearised Euler equations are solved in the time domain for the propagation step.

I. Introduction

Installation effects can no longer be neglected for new turbojets. Indeed, the optimisation of the propulsive efficiency requires to consider high-bypass-ratio turbofan engines, with a large fan diameter, installed close to the wings. Interactions of the jet flow with the wings produce an excess noise with respect to the same isolated jet. These additional acoustic sources must be taken into account in jet noise modelling. One of the first experimental study was undertaken by Mead and Strange[1]. They measured this excess noise for various wing geometries (a rectangular flat plate, a profile and a wing) in static conditions. An example of spectral decomposition, for a nozzle installed under a wing at 90° of the jet axis, is presented in Figure 1, for different azimuth angles ϕ. These angles are defined by the perpendicular plane to the jet axis. The cord of the wing is about 10 D and the trailing edge is located at 5.6 D of the ejection. They attributed the lower frequency component to the direct jet-wing interaction and the high frequency component to acoustic reflections. For a perfect reflection, a factor 2 can be observed on the spectra. However, for installed configurations, in Figure 1, there are lower deltas in high frequencies. These results were also observed recently in experimental results in Huber *et al.*[2] Phenomena present at high frequencies may be more complex like only reflection. Wang[3] and Shearin[4] studied the influence of geometrical parameters providing the relative position of the wing with respect to the jet. The flap deflection-angle as well as the radial and axial positions of the wing from the nozzle exit plane have been found to be the main parameters. Empirical models based on scaling laws have been proposed by Fink[5] and SenGupta[6]. Jet-flow modification, trailing edge noise and quadrupole noise from the deflected jet associated with impact noise, have been identified as the main noise sources. More recently, flight effects on jet-wing interaction noise have been studied by Miller[7] using a general statistical formulation.

An insightful numerical approach has also been performed by Pastouchenko and Tam[8]. They extended their statistical model[9,10] of jet mixing noise to include the presence of the wing flap, and obtained good predictions at high frequencies. More recently, a hybrid RANS/CAA computation, for a single stream jet in static condition placed under an airfoil and a deflected flap, has been done by Neifeld *et al.*[11]. The Tam & Auriault source model based on the contribution from the fine-scale jet mixing noise has been combined with

*Ph.D. student, Snecma, Rond-point René Ravaud, Réau, 77550 Moissy-Cramayel, France
†Research Engineer, Snecma, Rond-point René Ravaud, Réau, 77550 Moissy-Cramayel, France, AIAA Member
‡Professor, Ecole Centrale de Lyon, Senior AIAA Member

the linearised Euler equations to compute the sound propagation. A good agreement with measurements data is found except for the region where the flap is immersed in the jet flow. In the present study, installation effects are also investigated by using a RANS solution as input data in a statistical model. By this way, complex configurations are expected to be taken into account in an industrial framework[12]. A realistic turbofan jet engine placed under a NACA0012 profile without pylon and deflected-angle is here considered in what follows. Experimental data including the turbulent flow and its acoustics, are available for this configuration[13,14,15]. The acoustic step however needs to be revisited in this statistical approach. The free space assumption is no longer valid and the acoustic propagation is now performed by solving the linearised Euler equations.

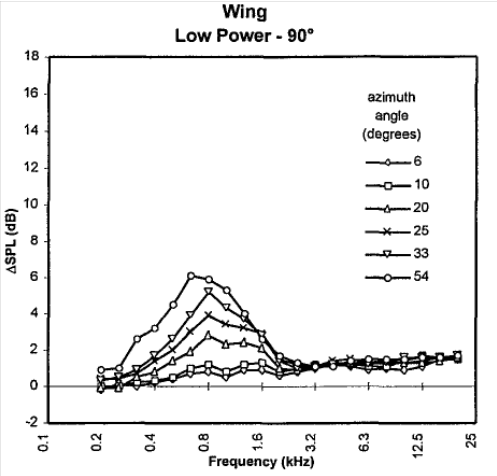

Figure 1. Spectral decomposition between installed and isolated configurations, for an installed single stream nozzle under a wing in static conditions for different azimuth angles, by Mead & Strange[1].

The paper is organised as follows. The methodology is described in Section 2. The isolated dual jet is presented in Section 3 and the installed configuration in Section 4. The acoustic modelling is reported in Section 5. Concluding remarks are provided in Section 6.

II. Methodology

A two-step approach is applied to predict installation effects on jet mixing noise. The flow modification due to the profile, presented by Fink[5] and SenGupta[6], will be illustrated by a RANS simulation of an installed nozzle. Jet noise sources associated with the fine-scale turbulence will be determined by the Tam & Auriault statistical model[9]. It is here assumed that the profile modifies the acoustic field generated by the jet (reflections and diffractions), but does not introduce dipolar sources. In other words, the profile is not located in the jet. The acoustical influence of the profile will be obtained by solving the linearised Euler equations.

The studied coaxial jet is defined by a hot core flow with a temperature $T_p = 829.4$ K, and a cold fan flow with $T_s = 342$ K. The primary Mach number is $M_p = 0.67$ and the secondary one is $M_s = 0.84$, with a nozzle diameter of $D_p = 0.13$ m and of $D_s = 0.22$ m respectively. The flight Mach number is $M_f = 0.27$. Two quantities are introduced : the mixing velocity $U = (U_p W_p + U_s W_s)(W_p + W_s)$, where U and W are respectively the velocity and the volum flow rate for primary and secondary flow; and the mixing diameter D defined by the methods described in SAE ARP 876 appendix F.

$$D = \left(\frac{4A}{\pi}\right)^{1/2} \tag{1}$$

where $A = A_p \rho_p U_p [1 + (W_s/W_p)]/(\rho U)$ is the mixed jet area. These quantities are built to assimilate double jet stream equivalent to a single jet flow at constant momentum, diameter D and velocity U .

The turbulent mean flow is computed by solving Reynolds-averaged Navier-Stokes equations combined with the $k-\omega$ BSL turbulence model of Menter[16], implemented in the elsA solver[17,18]. These equations are solved using a finite volume discretisation on structured grids[19]. Initial parameters retained for computation are the following : turbulent intensity is 1, 10 and 5 respectively for the external, fan and core flow, the quantity μ_t/μ is respectively 0.033, 100 and 10.

All CFD simulations are performed for a full three-dimensional geometry, and the simulation itself is carried out in two steps. First, the laminar solution is computed, corresponding to approximately 10,000 iterations, for the time-marching algorithm. The core and fan flows are initialised with a fictitious Mach number of 0.5, and the other blocks of the computational domain with the flight Mach number M_f. Second, the turbulent model is activated, and after a transient period, the simulation is performed until convergence.

Jet mixing noise predictions in free space are obtained by a statistical model formulated from the work by Tam & Auriault[9,10]. In this method, the adjoint problem is used to taking refraction effects into account. This new formulation is more computational efficient than a direct method. The acoustic power spectral density S of fine-scale turbulence for a far-field observer position $\boldsymbol{x}$ is described by

$$S(\mathbf{x},\omega) = 4\pi\Big(\frac{\pi}{\ln 2}\Big)^{3/2}\iiint \frac{\hat{q}_s^2 l_s^3}{c^2\tau_s}|p_a(\mathbf{x}_2,\mathbf{x}),\omega)|^2\frac{\exp\{-\omega^2 l_s^2/4u_c^2\ln 2\}}{[1+\omega^2\tau_s^2(1-u_c\cos\theta/a_\infty)^2]}d\mathbf{x}_2 \tag{2}$$

where ω is the angular frequency, $\mathbf{x}_2$ is the source position, p_a the adjoint pressure, u_c the convection velocity, ω the angle between the source and the observer, $\tau_s = c\tau k_t/\epsilon$ and $l_s = c_l k_t^{3/2}/\epsilon$ the time and space turbulent scales and $\hat{q}_s^2/c^2 = A^2(2/3\bar{\rho}k_t)^2$ the elementary source intensity. k_t stands for the turbulent kinetic energy and ϵ for its turbulent dissipation rate.

The adjoint pressure is evaluated in equation (3) by Tam[20] and Morris & Farassat[10] at $\theta = 90°$ where mean flow effects are negligible,

$$|p_a(\mathbf{x}_2,\mathbf{x},\omega)|^2 = \frac{\omega^2}{64\pi^4 c_0^4|\mathbf{x}-\mathbf{x}_2|^2} \tag{3}$$

A directivity factor $D(\theta) = (1-M_c\cos\theta)^{-3}$ needs to be introduced[21] if the adjoint pressure is not directly calculated. The acoustic power spectral density is then recast as follows

$$S(\mathbf{x},\omega) = \iiint D(\theta)S_{vol}(\mathbf{x},\omega)d\mathbf{x}_2 \tag{4}$$

$$= \iiint \frac{\sqrt{\pi}}{16\pi^2(\ln 2)^{3/2}\rho_0 c_0^5 x^2}D(\theta)\frac{\hat{q}_s^2 l_s^3}{c^2\tau_s}\omega^2\frac{\exp\{-\omega^2 l_s^2/4u_c^2\ln 2\}}{[1+\omega^2\tau_s^2(1-u_c\cos\theta/a_\infty)^2]}d\mathbf{x}_2 \tag{5}$$

An alternative to the use of the Green function consists in solving the linearised Euler equations. In Actran DGM, the flow is assumed to be isentropic, in the most general case, for a shear flow, and the acoustic field $(\rho', \boldsymbol{u}', p')$ is governed by[22]

$$\begin{cases} \dfrac{\partial}{\partial t}\rho' + \nabla.(U\rho' + c_0\rho) = 0 \\ \rho\Big(\dfrac{\partial}{\partial t} + U.\nabla\Big)\boldsymbol{u}' + \rho(\boldsymbol{u}'.\nabla)U + \rho'(U.\nabla)U = -\nabla p' \\ \dfrac{\partial p'}{\partial t} + \boldsymbol{u}'.\nabla p_0 = c_0^2(U.\nabla\rho)\Big(\dfrac{p'}{p_0} - \dfrac{\rho'}{\rho}\Big) \end{cases} \tag{6}$$

where p_0 is the constant pressure and ρ the mean density. Note that these equations are recast in a non-conservative convective form, and solved in a weak variational formulation. A source term can be added to the pressure equation.

The Tam & Auriault model, defined by equations (2) to (5), is implemented in the TAPIR tool developed by Snecma[12]. The propagation of the acoustic sources calculated with TAPIR is obtained by solving the linearised Euler equations in time domain. Consequently, mean flow effects on sound propagation as well as diffraction of jet noise by the wings can be computed.

III. Isolated nozzle case

As a preliminary study, CFD calculation is performed for an isolated nozzle. The meshing for this case is represented in Figure 2(a) for the half-nozzle, every block of the mesh being represented with a different color. The visualisation of the 2D plane of the nozzle is displayed in Figure 2(b). The mesh grid contains about 8 million cells. The size of the domain is 35D in the axial direction and 17D in the radial one. There is 132 points in the azimuthal direction. More than 20 nodes are necessary to correctly describe the turbulent profile of the boundary layer. The first cell at the wall is determined to satisfy $y^+ = yu_\tau/\nu = 1$.

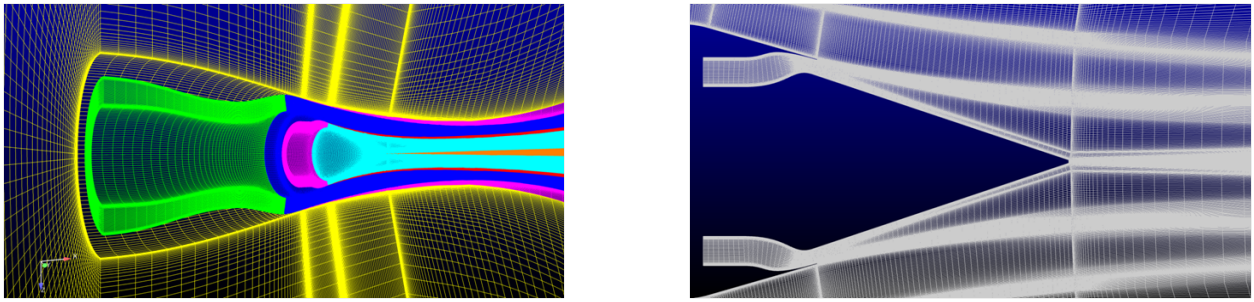

(a) (b)

Figure 2. Screenshot of the meshing for the isolated nozzle : (a) Visualisation of the half-nozzle, (b) Visualisation of the 2D plane.

Radial profile of the mean axial velocity, normalised by the mixing velocity U, for RANS calculation is compared to PIV measurements at $X/D = 3.3$ in Figure 3(a). This is the first plane available regarding PIV data. The origin $X/D = 0$ corresponds to the fan flow exit. The RANS calculation is represented as dashed curves and data are plotted in solid line. A good agreement is found for the secondary velocity but it is not the case for the primary one and the fan/external gradient. Thus, a resetting of the first plane is applied to the RANS solution to correctly compare this one with PIV measurements. Two close planes are plotted in Figure 3(b) : one at $X/D = 3.5$ and the other at $X/D = 4.2$. The first plane is appropriate to obtain the fan/external gradient and the plane at $X/D = 4.2$ is suitable to correctly capture the maximum of the mean axial velocity. The reference plane chosen here, for the RANS calculation, is located at $X/D = 4.2$.

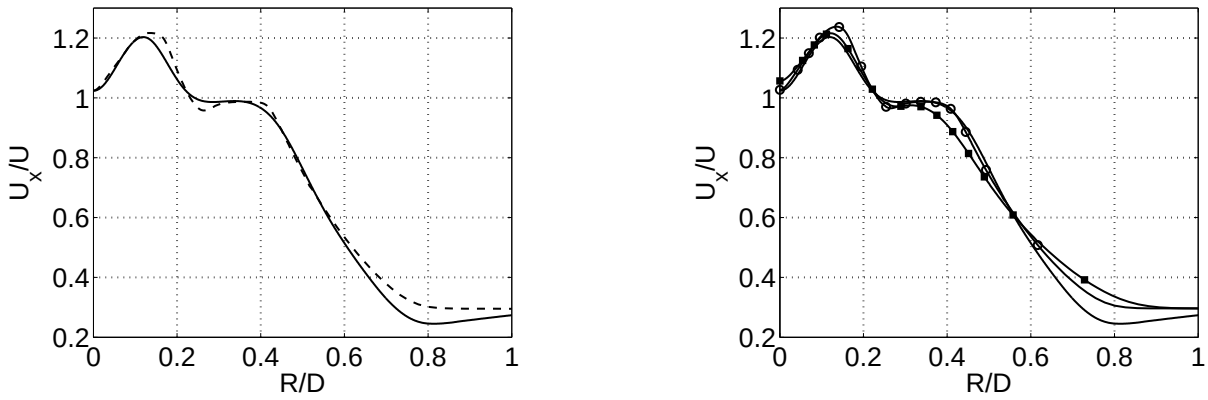

(a) — PIV measurements, **- -** RANS plane at $X/D = 3.3$.

(b) — PIV measurements, -o- RANS plane at $X/D = 3.5$, -■- RANS plane at $X/D = 4.2$.

Figure 3. Mean axial velocity, normalised by the mixing velocity U, in the radial direction for PIV plane at $X/D = 3.3$ compared with close planes for RANS calculation.

The evolution of the velocity in the radial direction for two planes, one close to the fan nozzle exit and the other close to the end of potential core at $X/D = 10$, is displayed in Figure 4 for the RANS calculation and PIV data. It is recalled that there is an axial shift of 0.9D between PIV and RANS planes. Despite the

large size of the potential core at $X/D = 10$, calculation results are in good agreement with measurements. These results highlight the shortcomings in the calculations, namely the bad prediction of the potential core length, associated with difficulties to get a correct mixing noise.

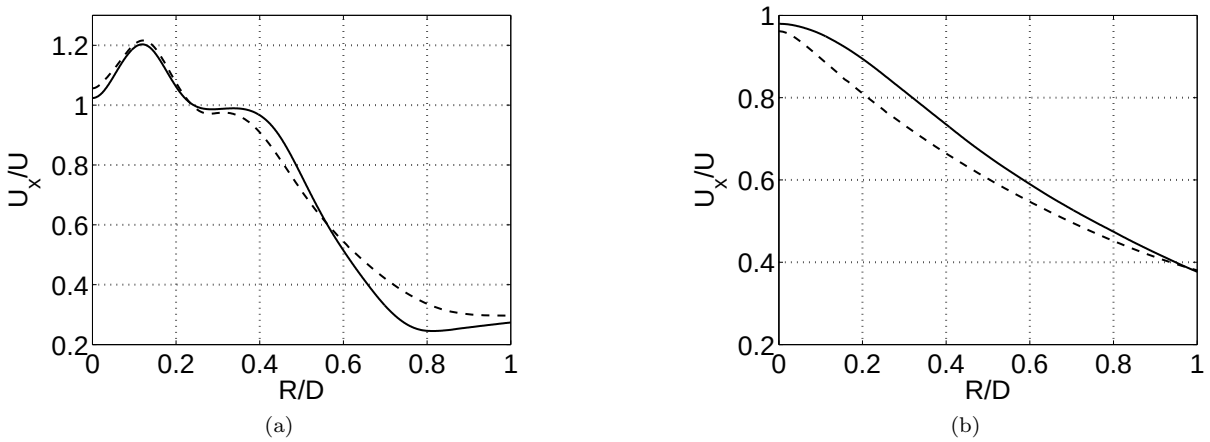

Figure 4. Mean axial velocity in the radial direction, — PIV measurements, - - RANS calculation : (a) $X/D = 3.3$ for the PIV plane, (b) $X/D = 10$ for the PIV plane.

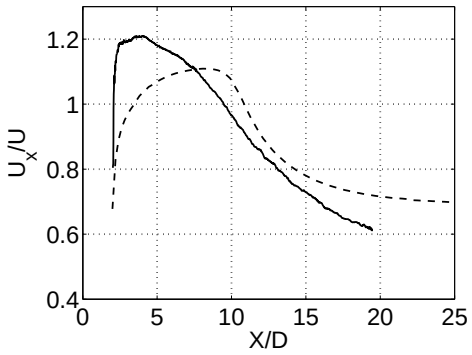

Figure 5. Mean axial velocity in the axial direction on the jet axis, — PIV measurements, - - RANS calculation.

The mean axial velocity in the axial direction along the jet axis is plotted in Figure 5. The potential core, for the RANS calculation, is found to be higher than the PIV data one. It is a calculation shortcoming presented previously.

Turbulent kinetic energy (k_t) in the radial direction at $X/D = 3.3$ and $X/D = 10$ is plotted in Figure 6 for PIV data and the RANS calculation. PIV results slightly vary with the size of the analysis window. In this test campaign, the reduction of the window increases measurement noise. This phenomenon is documented in the paper by David *et al.*[14]. This explains the important difference between the RANS calculation and PIV data. Therefore, the calculation validation cannot be done on k_t. However, the maximum for the turbulent kinetic energy is correctly predicted at $X/D = 4.7$. These cartographies are shown in Figure 7 for RANS calculation and PIV measurements.

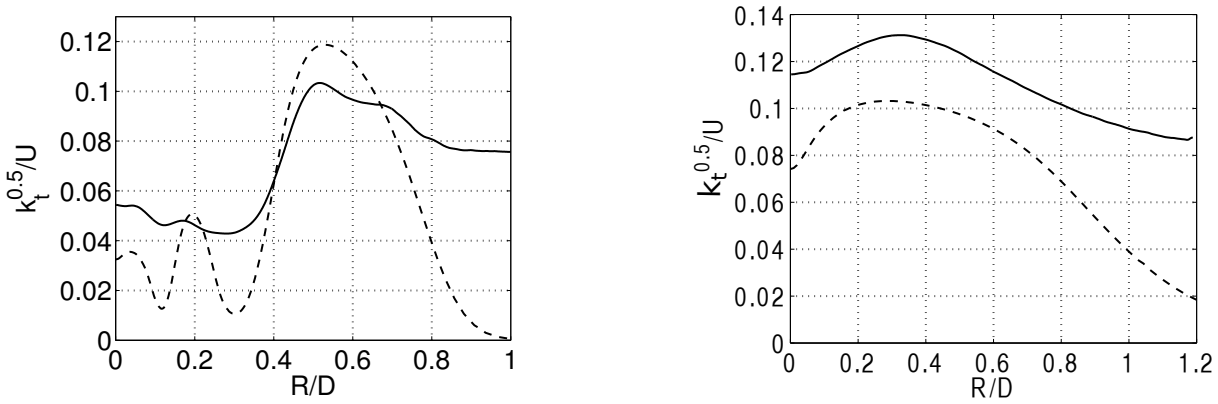

(a) (b)

Figure 6. Turbulent kinetic energy profile in the radial direction, — PIV measurements, - - CFD calculation : (a) $X/D = 3.3$ for the PIV plane, (b) $X/D = 10$ for the PIV plane.

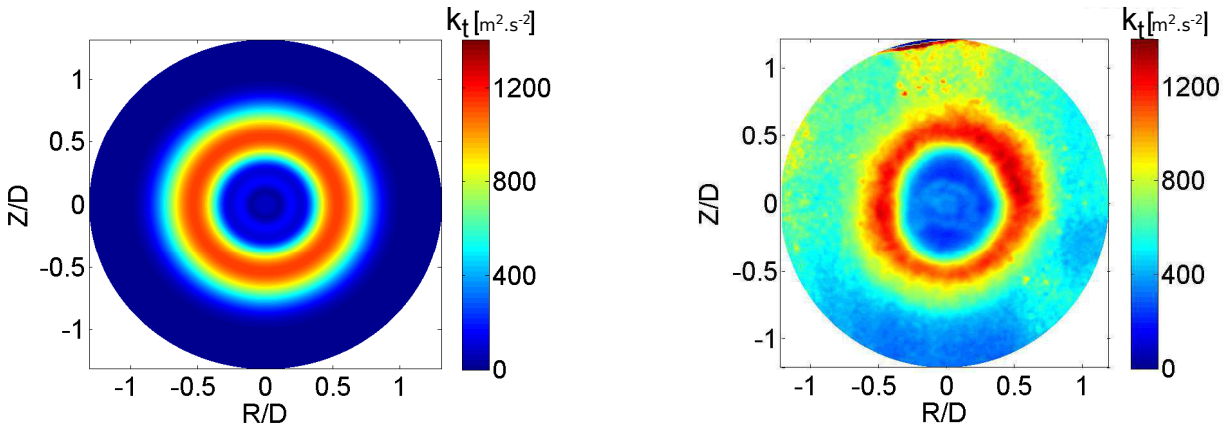

(a) (b)

Figure 7. Turbulent kinetic energy cartography in the radial direction at $X/D = 4.7$: (a) RANS calculation, (b) PIV measurements.

The TAPIR solver is used to predict the jet mixing noise of the isolated nozzle case, as described previously, and to provide acoustical sources. The sound pressure level at 90° from the jet axis and the overall sound pressure level are displayed in Figure 8. In static condition, a good agreement is found with the model except for the maximum of SPL, where a frequency offset is observed. In flight condition, the frequency offset is more important but the amplitude difference between static and flight conditions for the data and TAPIR prediction is the same. So, a good agreement with measurements is found, except for the directivity in flight condition. The localisation of jet noise sources, which depends on frequency, is shown in Figure 9. For higher frequencies, sources localised in the shear layers will be increasingly close to the ejection nozzle. This result is in agreement with the experiments performed by Fleury & Davy[15]. PIV and acoustic data allowed to validate RANS calculation for the isolated nozzle case.

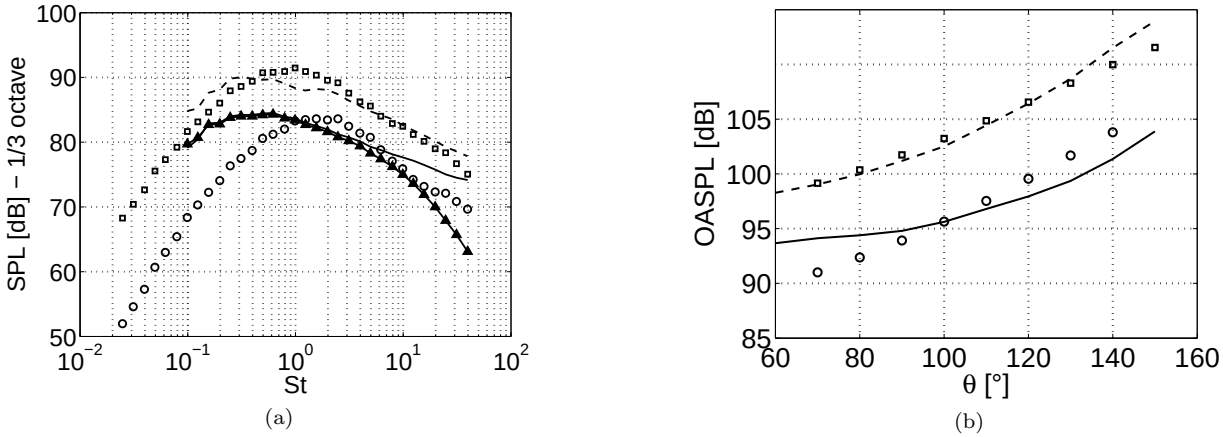

(a) (b)

Figure 8. TAPIR results : (a) SPL at 90 ° , (b) OASPL, — data in flight condition, ▲ data in flight condition with angular correction, ○ TAPIR in flight condition, - - data in static condition, □ TAPIR in static condition.

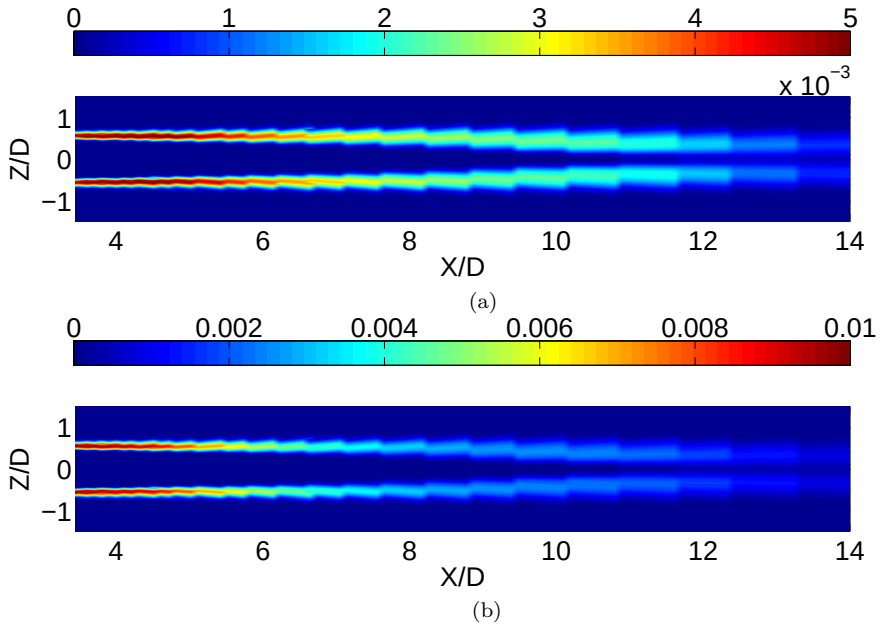

(a) (b)

Figure 9. Map of jet noise sources calculated from TAPIR for two frequencies : (a) 500Hz, (b) 1000Hz.

IV. Installed nozzle case

The nozzle is placed under a NACA0012 profile without incidence and pylon. This configuration is represented in Figure 10(a). The effect of the deflected-angle is neglected which allows only to consider the profile impact on the jet flow. NACA profile is localised for $Z/D > 0$ and its trailing edge is not immersed in the jet flow. For this configuration, there are no PIV measurement. Installed results will be compared with the isolated nozzle CFD calculation because there is no PIV measurements for installed nozzle. The mesh of the nozzle and the jet development, displayed in Figure 10(b), is very similar to the isolated one. The same numerical criteria are retained. The computation domain has about 13 million cells and the value $y^+ = 1$ at the wall is satisfied.

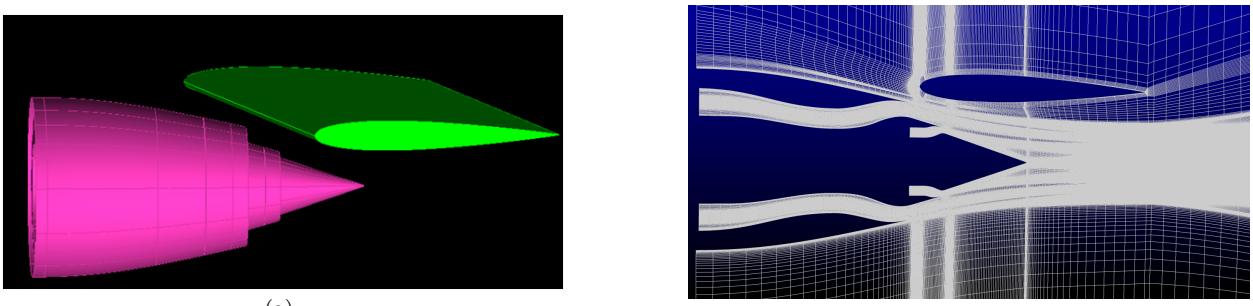

(a) (b)

Figure 10. Screenshots of the meshing tool for the installed nozzle : (a) Visualisation of the geometry, (b) Visualisation of the mesh in the plane y = 0.

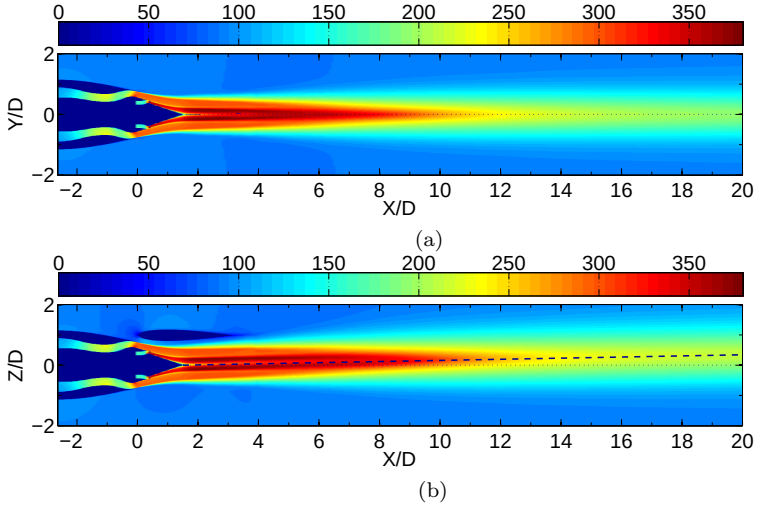

Figure 11. Mean axial velocity cartography in the axial direction for the installed nozzle : (a) xy plane (z = 0), (b) xz plane (y = 0).

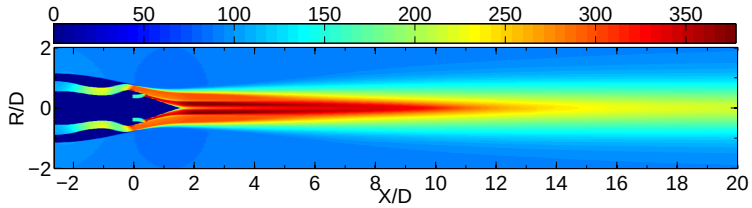

Figure 12. Computed mean axial velocity in the axial direction for the isolated nozzle case.

The mean axial velocity cartography in the axial direction for the installed nozzle case is displayed in Figure 11. Two planes are represented : (a) the parallel plane to the NACA, i.e. for $Z/D = 0$ and (b) the perpendicular one for $Y/D = 0$. The same cartography for the isolated nozzle is shown in Figure 12. The jet development for the installed nozzle is close to the isolated one, but the jet flow is significantly deflected by the NACA. The dashed curve in Figure 11(b) corresponds to the peak of velocity in each radial section, and illustrates this asymmetry. The mean axial velocity along the jet axis is plotted in Figure 13. The velocity of the isolated nozzle is represented in solid black curve. The solid white circles define the velocity for the installed case taken for $Z/D = 0$ whereas the dashed curve is for the deviated jet. The comparison between both actual axis jet for isolated and installed cases cannot be representative because the jet is deflected by the profile. However velocity, for the deviated jet, is similar to the isolated nozzle case results. Mean axial velocity cartographies at $X/D = 5.6$ for both cases are presented in Figure 14. This plane is near the

trailing edge of the NACA. The wake of the profile and a slight jet deflection can be observed in Figure 14(b). Thus, the effect of the profile on the jet flow for the mean axial velocity is the deflection of the jet. This phenomenon was illustrated in Dezitter *et al.*[23], where CFD calculations were performed on a very high by-pass ratio nozzle installed under a wing with a pylon.

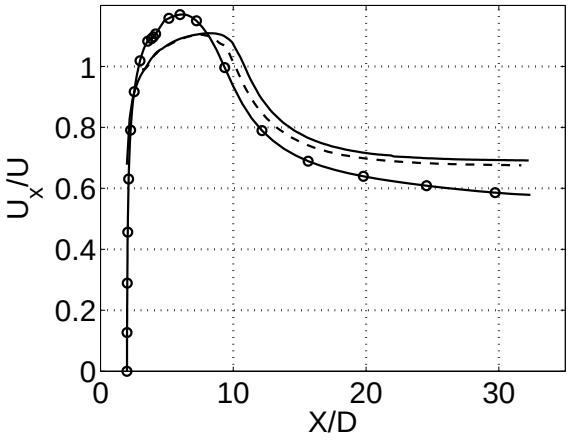

Figure 13. Computed mean axial velocity profile on the jet axis (R/D = 0) : — Isolated case, -o- Installed case (geometric axis jet), - - Installed case (actual axis jet, described in the Figure 11(b)).

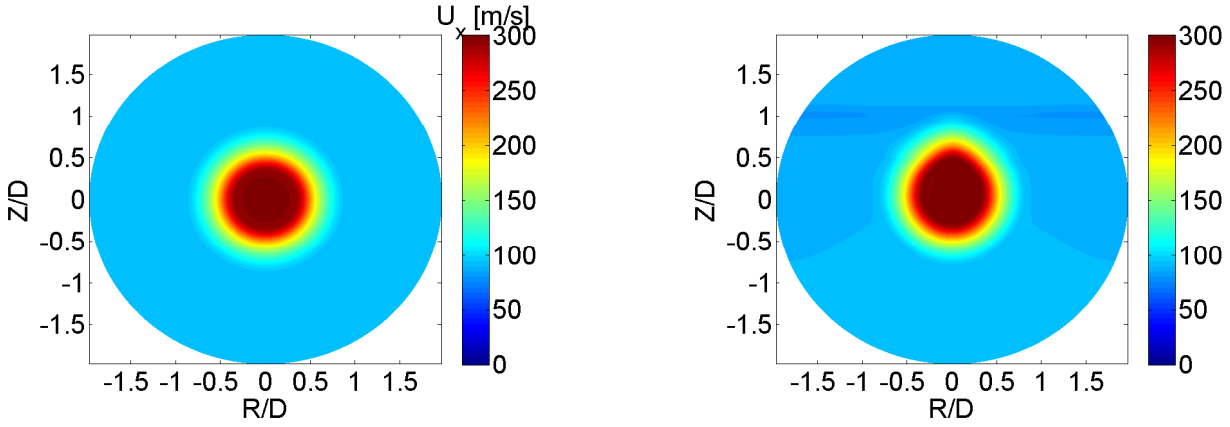

Figure 14. Mean axial velocity cartography at $X/D = 5.6$ for CFD calculation : (a) Isolated nozzle case, (b) Installed nozzle case.

The turbulent kinetic energy cartography in the axial direction is shown in Figure 15 for two planes : one parallel and one perpendicular to the NACA profile. There is a deficit of the turbulent kinetic energy in the vicinity of the NACA profile, refer to Figure 15(b). However, there is no influence of the profile on the opposite side of the nozzle ($Z/D < 0$), which is an interesting result of the impact of the profile. This effect can also be observed in Figure 16 which k_t profile in axial direction for isolated and installed case is represented. The turbulent kinetic energy for the isolated nozzle is displayed in solid curve. The k_t profile extracted to the xz plane is plotted in blank circles, whereas, the k_t profile of the xy plane is represented by black squares. In the vicinity of the NACA profile, the turbulent kinetic energy is less important than without installation. In addition to this phenomenon there is also a jet deflection, displayed in Figure 17. Except for the jet deflection, turbulent kinetic energy on the jet axis is similar with and without NACA profile. Thus, the NACA effect on k_t is a deviated jet as for the velocity and a deficit in the vicinity of the profile.

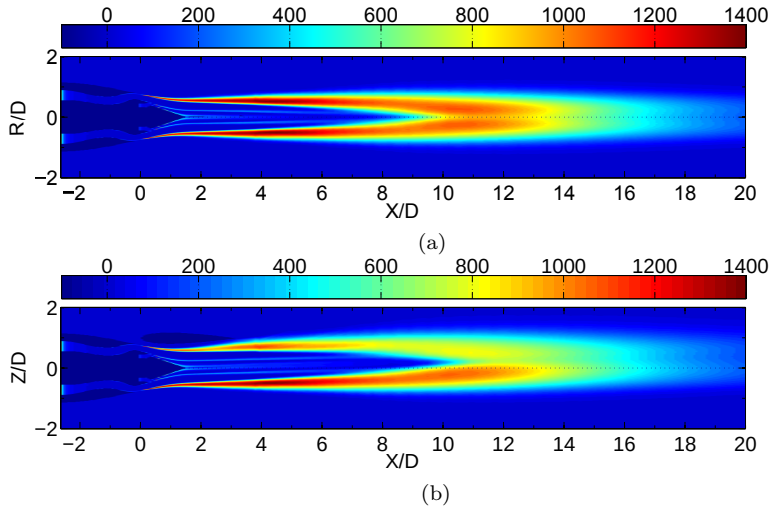

Figure 15. Turbulent kinetic energy cartography in the axial direction for the installed nozzle : (a) xy plane (z = 0), (b) xz plane (y = 0).

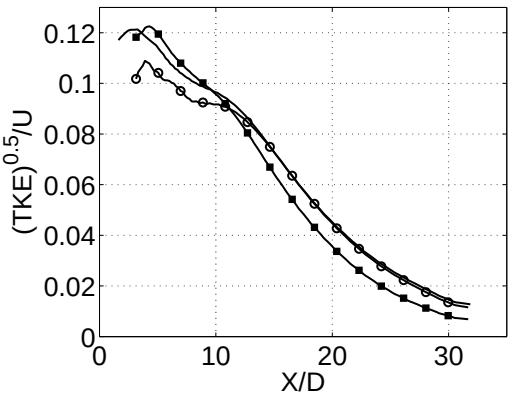

Figure 16. Turbulent energy kinetic in the shear layers ($Z/D = \pm 0.5$) in axial direction : — Isolated CFD, -o- $Z/D = 0.5$ for installed CFD, i.e. at the trailing edge, -■- $Z/D = -0.5$ for installed CFD. The offset between isolated and installed cases for X/D is due to the presence of the NACA and the creation of cartographies in axial direction, refer to Figs. 11 and 15.

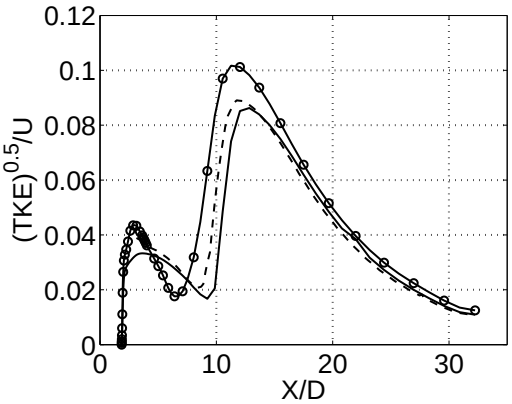

Figure 17. Turbulent energy kinetic on the jet axis (R/D = 0) : — Isolated CFD, -o- Installed CFD (geometric axis jet), - - Installed CFD (actual axis jet, described in the Figure 11(b)).

V. Acoustic modelling

The acoustical propagation is realised by the Actran DGM solver. The finite and infinite element method[22] and discontinuous Galerkin method are used. Only unstructured tetrahedral meshes are supported : a new mesh has to be generated (Figure 18). There is a physical domain which contains the geometry, a non-reflecting boundary condition and a buffer zone, with a thickness of a wavelength, for the damping of acoustic waves. No acoustic phenomenon are existing in the nozzle, therefore it is represented by a cylinder with a size of λ for avoid reflections. Cell size L depends on the mean flow velocity U by : $L = 1.5\lambda_c$ where $\lambda_c = (c - U)/f$[22]. It is to respect an order of 6 for the discontinuous Galerkin method. Different domains are therefore created : primary and secondary jets and the external domain. The mesh grid contains about 400 million cells.

CFD mean flow calculated previously is used as Actran DGM input. A mean flow interpolation on the

tetrahedral mesh is performed : cartographies of mean axial velocity and pressure interpolated are presented in Figure 19.

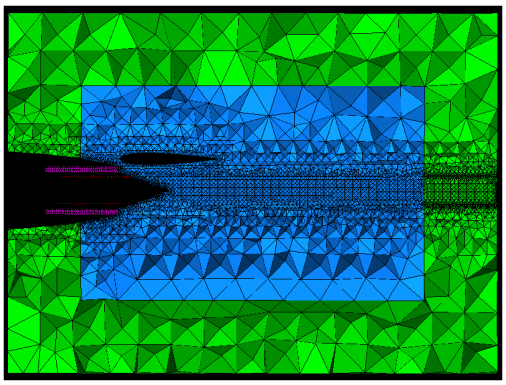

Figure 18. 2D plane tetrahedral mesh of the installed nozzle. Physical domain is represented in blue and buffer zone in green..

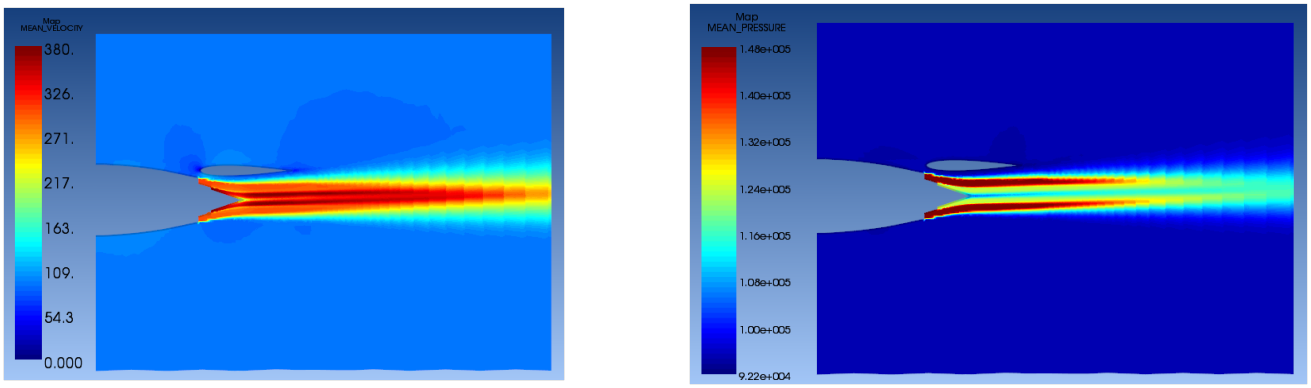

(a) Mean axial velocity

(b) Pressure

Figure 19. Installed CFD flow interpolation on the tetrahedral acoustic mesh : 2D plane of the mean axial velocity U_X (a) and the mean pressure (b).

A first test case of a monopole in free space is considered, located in a quiescent uniform medium on the one hand, and in an uniform subsonic mean flow on the other hand. The free space scalar Green's function G_0 in the presence of uniform subsonic mean flow is given by[22,24,25].

$$G_0(k_0,R,t)=\frac{1}{i\omega c_0^2 4\pi}\frac{\exp\left\{ik_0\left[\left(\frac{R^2}{1-M^2}+\frac{M^2(\boldsymbol{x}-x_s)^2}{(1-M^2)^2}\right)^{1/2}-\frac{M(\boldsymbol{x}-x_s)}{1-M^2}\right)\right]\right\}}{\left(R^2+\frac{M^2(\boldsymbol{x}-x_s)^2}{1-M^2}\right)^{1/2}\sqrt{1-M^2}}\exp(-i\omega t) \tag{7}$$

where R is the source-observer distance, $k_0=\omega/c_0$ and x_s the source location. The acoustic pressure is related to the convective derivative of the Green's function G_0

$$p'=\left(\frac{\partial}{\partial t}+c_0M\nabla.\right)G_0 \tag{8}$$

In a quiescent uniform medium, the equations (7) and (8) become

$$\begin{cases} G_0(k_0,R,t)=\dfrac{1}{i\omega c_0^2 4\pi}\dfrac{\exp(ik_0R)}{R}\exp(-i\omega t) \\ p'=-i\omega G_0 \end{cases} \tag{9}$$

The Actran source is defined by

$$G(k_0, R, t) = A\frac{\exp(ik_0R)}{R}\exp(-i\omega t) \tag{10}$$

Thus, these two Green's functions are connected by $A = -4\pi c_0^2$. An example of a monopole radiation, for $A = 1$ and the frequency $f = 1000$ Hz is described in Figure 20. Analytical and numerical solutions are plotted on the source axis, and similar results are obtained.

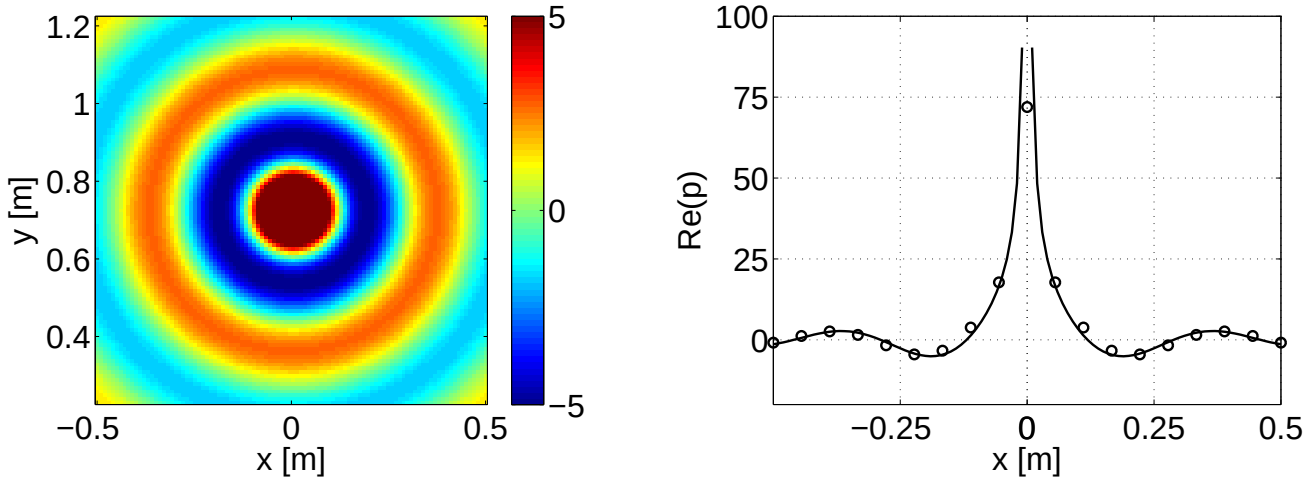

(a) (b)

Figure 20. Monopole radiation in free space without mean flow: (a) cartography of real part of the pressure for analytical solution, (b) profile on the source axis ($y = y_s$, where y_s is the source location) for ∘ Actran DGM and — analytical solution (equation 9).

Figure 21 represents the same monopole in an uniform subsonic mean flow and there is a good agreement between numerical and analytical results, except very close to the monopole.

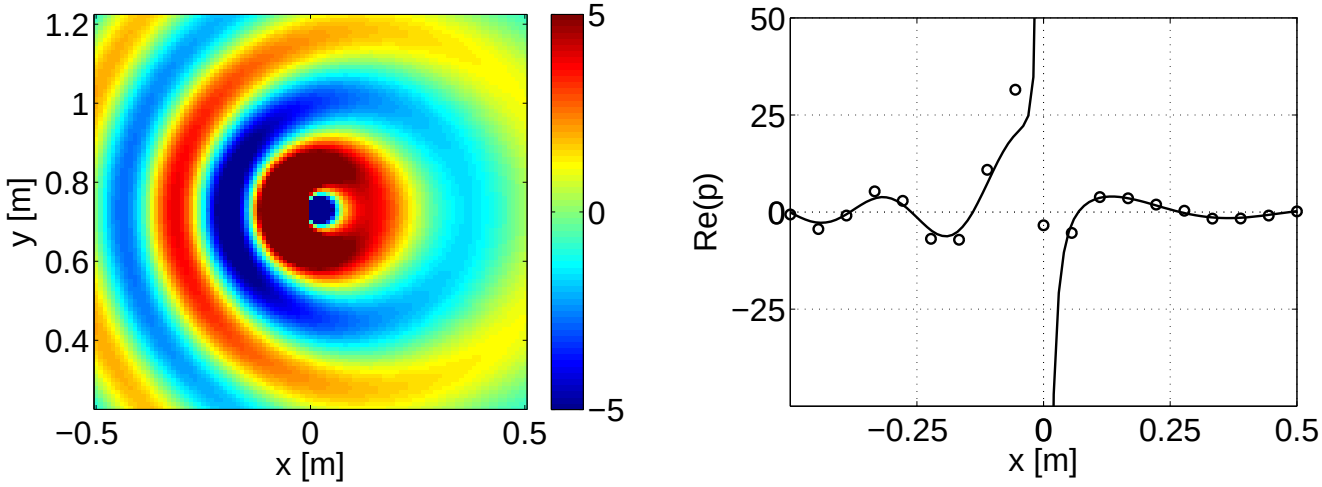

(a) (b)

Figure 21. Monopole radiation in free space in uniform subsonic mean flow ($M_j = 0.29$) : (a) cartography of real part of the pressure for analytical solution, (b) profile on the source axis for ∘ Actran DGM and — analytical solution.

Now, the same monopole is located in the CFD mean flow. The cartography of the pressure is presented in Figure 22. There is a shielding effect of the radiation due to the NACA profile. An instability wave appears with the resolution of linearised Euler equations in time domain for low frequencies on the jet axis.

By passing the problem in the frequency domain, the growth of the instability wave is prevented[26]. This phenomenon is physical and it can overwhelm the acoustic propagation but there is an other way, described by Bogey *et al.*[27], to eliminate this instability. It comes to remove the gradient terms, which correspond to vortical modes. Thus, the second equation of the system (6) can be rewritten by

$$\rho\Big(\frac{\partial}{\partial t} + U.\nabla\Big)\boldsymbol{u}' = -\nabla p' \tag{11}$$

Now, this equation is purely acoustics. The next step of this study will consist of the propagation or TAPIR sources in the CFD jet flow. A monopole distribution, coming from TAPIR results, will be displayed in the flow field, with corresponding source amplitude, and the propagation will then be carried out.

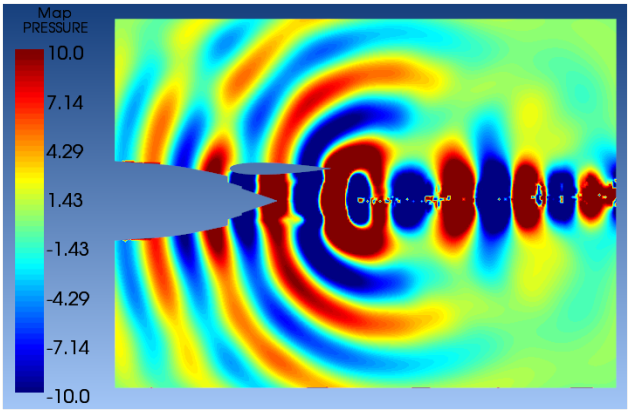

Figure 22. Real part of the pressure for the acoustical propagation of a monopole with an amplitude $A = 1$ and a frequency $f = 1000$ Hz in CFD mean flow.

VI. Conclusion

RANS simulations of an isolated and installed nozzle are performed. For the isolated case, results are compared with PIV measurements. Despite data incertitude for the turbulent kinetic energy, CFD calculations are found in good agreement with measurements. For the installed case, a NACA profile without incidence is considered. The pylon is not considered in this study. These results are compared with the isolated nozzle calculation. The impact of the NACA over the jet flow is highlighted. The jet flow is deflected and a deficit of the turbulent kinetic energy near the NACA profile is observed. The acoustic approach, based on the linearised Euler equations, is to propagate a monopole in the CFD flow. An instability wave appeared in the acoustic results, but it is possible to remove it. The strategy employed will consist to identify the position of the sources, determined by TAPIR. Acoustical sources will be extracted to be included in the jet flow interpolated with Actran DGM solver.

References

[1]Mead, C. J. and Strange, P. J. R., "Under-wing installation effects on jet noise at sideline," No. 1998-2207, 4th AIAA/CEAS Aeroacoustics Conference, 1998.

[2]Huber, J., Drochon, G., Pintado-Peno, A., Cléro, F., and Bodard, G., "Large-scale jet noise testing , reduction and methods validation EXEJET : 1 . Project overview and focus on installation," AIAA Paper, , No. 3032, 2014.

[3]Wang, M. E., "Wing effect on jet noise propagation," Journal of Aircraft, Vol. 18, No. 4, 1981, pp. 295–302.

[4]Shearin, J. G., "Investigation of jet-installation noise sources under static conditions," Tech. rep., NASA, 1983.

[5]Fink, M. R., "Propulsive lift noise," Aeroacoustics of flight vehicles : Theory and practice, Volume1 : Noise, edited by H. H. Hubbard, 1991, pp. 449–481.

[6]SenGupta, G., "Analysis of jet-airframe interaction noise," No. 1983-0783, 8th Aeroacoustics Conference, 1983.

[7]Miller, W. R., "Flight effects for jet-airframe interaction noise," No. 0784, 8th AIAA Aeroacoustics Conference, 1983.

[8]Pastouchenko, N. N. and Tam, C. K., "Installation Effects on the Flow and Noise of Wing Mounted Jets," AIAA Journal, Vol. 45, No. 12, Dec. 2007, pp. 2851–2860.

[9]Tam, C. K. W. and Auriault, L., "Jet mixing noise from fine-scale turbulence," AIAA Journal, Vol. 37, No. 2, Jan. 1999, pp. 145–153.

[10]Morris, P. J. and Farassat, F., "Acoustic Analogy and Alternative Theories for Jet Noise Prediction," AIAA Journal, Vol. 40, No. 4, April 2002, pp. 671–680.

[11]Neifeld, A., Ewert, R., Keller, D., and Steger, M., "Towards prediction of jet noise installation effect using stochastic source modeling," No. 3059, 20th AIAA/CEAS Aeroacoustics Conference, 2014.

[12]Bodard, G., Bailly, C., and Vuillot, F., "Matched hybrid approaches to predict jet noise by using Large-Eddy Simulation," No. 2009-3316, 15th AIAA/CEAS Aeroacoustics Conference (30th AIAA Aeroacoustics Conference), 2009.

[13]Huber, J., Drochon, G., Pintado-Peno, A., Cléro, F., and Bodard, G., "Large-scale jet noise testing, reduction and methods validation "EXEJET": 1. Project overview and focus on installation," No. 2014-3032, AIAA/CEAS Aeroacoustics Conference (20th AIAA/CEAS Aeroacoustics Conference), 2014.

[14]David, F., Jourdan, J.-M., Cléro, F., Koenig, M., and Huber, J., "Large-scale jet noise testing, reduction and methods validation "EXEJET": 4. Flows characterization with PIV in the CEPRA19 anechoic wind tunnel of Onera," No. 2014-3035, AIAA/CEAS Aeroacoustics Conference (20th AIAA/CEAS Aeroacoustics Conference), 2014.

[15]Fleury, V. and Davy, R., "Large-scale jet noise testing, reduction and methods validation "EXEJET": 5. Analysis of jet-airfoil interaction noise by microphone array techniques," No. 2014-3036, AIAA/CEAS Aeroacoustics Conference (20th AIAA/CEAS Aeroacoustics Conference), 2014.

[16]Menter, F. R., "Influence of freestream values on $k - \omega$ turbulence model predictions," AIAA Journal, Vol. 30, No. 6, 1992, pp. 1657–1659.

[17]Reneaux, J., Beaumier, P., and Girodroux-Lavigne, P., "Advances aerodynamic applications with the elsA software," The Onera Journal Aerospace Lap, 2011.

[18]Cambier, L. and Veuillot, J.-P., "Status of the elsA CFD software for simulation and multidisciplinary applications," No. 664, 46th AIAA Aerospace Sciences Meeting and Exhibit, 2008.

[19]Lazareff, M. and Cambier, L., "elsA's theoretical manual," Tech. rep., Onera, 2004.

[20]Tam, C. K., "Dimensional Analysis of Jet Noise Data," AIAA Journal, Vol. 44, No. 3, March 2006, pp. 512–522.

[21]Goldstein, M. E., Aeroacoustics, mcGraw-Hill ed., 1976.

[22]Free Field Technologies SA, Actran DGM 14.0 User's guide, 2013.

[23]Dezitter, F., Bezard, H., de Saint Victor, X., Zeggai, K., Britchford, K., Joubert, G., and Puigt, G., "Installation effects characterization of VHBR engines Part III : CFD assessment for jet mixing," AIAA Paper, , No. 3370, 2009.

[24]Bailly, C. and Juvé, D., "Numerical solution of acoustic propagation problems using linearized Euler equations," AIAA Journal, Vol. 38, No. 1, 2000, pp. 22–29.

[25]Zhenlin, J., Qiang, M., and Zhihua, Z., "Application of the boundary element method to predicting acoustic performance of expansion chamber mufflers with mean flow," Journal of Sound and Vibration, Vol. 173, No. 1, 1994, pp. 57–71.

[26]Agarwal, A., Morris, P. J., and Mani, R., "Calculation of sound propagation in nonuniform flows : suppression of instability waves," AIAA Journal, Vol. 42, No. 1, Jan. 2004, pp. 80–88.

[27]Bogey, C., Bailly, C., and Juvé, D., "Computation of flow noise using source terms in Linearized Euler's Equations," AIAA Journal, Vol. 40, No. 2, 2002, pp. 235–243.